

Tidal impact on the division of river discharge over distributary channels in the Mahakam Delta

Maximiliano G. Sassi · A. J. F. Hoitink ·
Benjamin de Brye · Bart Vermeulen ·
Eric Deleersnijder

Received: 31 January 2011 / Accepted: 11 July 2011 / Published online: 7 August 2011
© Springer-Verlag 2011

Abstract Bifurcations in tidally influenced deltas distribute river discharge over downstream channels, asserting a strong control over terrestrial runoff to the coastal ocean. Whereas the mechanics of river bifurcations is well-understood, junctions in tidal channels have received comparatively little attention in the literature. This paper aims to quantify the tidal impact on subtidal discharge distribution at the bifurcations in the Mahakam Delta, East Kalimantan, Indonesia. The Mahakam Delta is a regular fan-shaped delta, composed

of a quasi-symmetric network of rectilinear distributaries and sinuous tidal channels. A depth-averaged version of the unstructured-mesh, finite-element model second-generation Louvain-la-Neuve Ice-ocean Model has been used to simulate the hydrodynamics driven by river discharge and tides in the delta channel network. The model was forced with tides at open sea boundaries and with measured and modeled river discharge at upstream locations. Calibration was performed with water level time series and flow measurements, both spanning a simulation period. Validation was performed by comparing the model results with discharge measurements at the two principal bifurcations in the delta. Results indicate that within 10 to 15 km from the delta apex, the tides alter the river discharge division by about 10% in all bifurcations. The tidal impact increases seaward, with a maximum value of the order of 30%. In general, the effect of tides is to hamper the discharge division that would occur in the case without tides.

Responsible Editor: Chari Pattiaratchi

This article is part of the Topical Collection on *Physics of Estuaries and Coastal Seas 2010*

M. G. Sassi (✉) · B. Vermeulen · A. J. F. Hoitink
Hydrology and Quantitative Water Management Group,
Department of Environmental Sciences, Wageningen
University, Droevendaalsesteeg 4, Wageningen, Gld,
The Netherlands
e-mail: maximiliano.sassi@wur.nl

B. de Brye · E. Deleersnijder
Institute of Mechanics, Materials and Civil Engineering
(IMMC), Université Catholique de Louvain,
4 Avenue G. Lemaître, Bte L4.05.02, 1348
Louvain-la-Neuve, Belgium

B. de Brye · E. Deleersnijder
Earth and Life Institute (ELI), G. Lemaître Centre
for Earth and Climate Research (TECLIM), Université
Catholique de Louvain, 2 Chemin du Cyclotron,
1348 Louvain-la-Neuve, Belgium

A. J. F. Hoitink
Institute for Marine and Atmospheric Research Utrecht
(IMAU), Department of Physical Geography, Utrecht
University, Utrecht, The Netherlands

Keywords Subtidal dynamics · Finite elements ·
River-tide interaction · Hydrodynamic model ·
Deltas · Mahakam · River discharge ·
Differential water level setup

1 Introduction

Most of the world's large rivers debouch in deltas prograding on continental shelves. Flow division in delta channel networks may affect the occurrence of natural resources in coastal areas, as river discharges carry terrestrial sediments, nutrients and contaminants to the coastal zone. Discharge division at bifurcations may

assert a strong control over the morphological evolution of river deltas (Wolinsky et al. 2010), as the flow brings the material needed for delta progradation (Edmonds and Slingerland 2007). Coastal ecosystems may depend on the organic matter brought by the river, whose main pathways are controlled by flow processes at bifurcations in the delta. The processes governing flow division at river bifurcations have been investigated theoretically (Wang et al. 1995; Bolla-Pitaluga et al. 2003), with numerical models (Lane and Richards 1998; Dargahi 2004; Zanichelli et al. 2004), and in experimental flumes (Bertoldi and Tubino 2007). These studies generally do not consider the influence of tides, which intrude from the mouths of distributaries and complicate the processes governing flow division (Buschman et al. 2010). The aim of this paper is to investigate the tidal impact on the distribution of river discharge over the distributary channels of a tidally influenced delta.

In shallow rivers, frictional forces generally exceed forces associated with inertial accelerations. Therefore, fortnightly fluctuations in water level arise as a consequence of fortnightly variation in friction (LeBlond 1979; Godin 1991). Buschman et al. (2009) decomposed the tidally averaged friction term (herein subtidal friction) into contributions due to (1) river discharge, (2) river-tide interaction and (3) tidal asymmetry inherent to the sum of tidal harmonics. Subtidal friction is mainly balanced by the pressure gradient, which leads to the characteristic subtidal variation in water level. Buschman et al. (2009) used their analysis of the subtidal momentum balance to explain subtidal water level dynamics in the Berau River, East Kalimantan, Indonesia. Motivated by observations at the apex of the Berau Delta, Buschman et al. (2010) investigated the sensitivity of subtidal flow division to tidal modulation. An idealized numerical model was setup of a river that bifurcates in two sea-connected branches, with parameters resembling those in the real case. Numerical experiments were conducted to investigate the sensitivity of subtidal flow division to variations in depth, length, width and bed roughness of one of the bifurcating branches. Buschman et al. (2010) highlighted the importance of tides in enhancing the inequality in subtidal flow division when one of the sea-connected branches was deeper or shorter, whereas bed roughness differences resulted in an opposing effect. The aforementioned idealized study awaits confirmation from studies of delta distributary networks based on full-complexity models, such as presented herein.

A tidal wave that propagates upriver as a progressive wave induces a landward mass transport known as Stokes flux. The Stokes flux is maximal when wa-

ter surface level and flow velocity are in phase, and reduces when the phase difference approaches 90° . Stokes fluxes in tidal channels therefore may be negligible when the effect of friction balances the effect of width convergence, such that the tidal wave resembles a standing wave (Friedrichs and Aubrey 1994). In a single channel, the Stokes flux is compensated by a seaward directed flux (hereinafter return flux), induced by a subtidal pressure gradient. When two channels join at a bifurcation, the system is constrained by one water surface level, although flow velocity amplitudes and phases may differ. The landward Stokes flux at each of the channels induces a return flow that does not necessarily balance in each individual channel. The asymmetry in the return flow therefore enhances a tidal mean discharge into one of the downstream channels.

Studies on tidal distributary networks often address problems with numerical models, owing to the complexity of the systems and the impossibility to monitor relevant spatial and temporal scales comprehensively. The insights from the existing literature is therefore fragmented. In the Columbia River estuary, Lutz et al. (1975) observed that for low river discharge, tides caused an asymmetrical flow distribution during the ebb. Hill and Souza (2006) showed that continuity and momentum equations may be linearized for a network of deep channels. They successfully represented tidal propagation in a fjord region. In a channel network forced by tides at entrances on opposite sides Warner et al. (2003) showed that subtidal flows are controlled by the temporal phasing and spatial asymmetry of the two forcing tides. Buijsman and Ridderinkhof (2007) showed that subtidal flows in the shallow Wadden Sea occur between the inlet channels that have a large tidal range and inlets with lower tidal range, reflecting the effect of nonlinearities in the shallow water equations.

The tidal motion in delta channel networks is characterized by a wide range of temporal and spatial scales, which becomes even wider when river dynamics and the transient interactions with the tidal motion are taken into account. Unstructured-mesh modeling is a promising option to deal with multi-scale physics in space and time (e.g. Deleersnijder et al. 2010). The main advantage is the spatial flexibility with a possible refinement in small channels, in shallow areas or across inclined bottoms. The Second-generation Louvain-la-Neuve Ice-ocean Model (SLIM, www.climate.be/slim) is able to cope with highly multi-scale applications (Deleersnijder and Lermusiaux 2008; Lambrechts et al. 2008a) such as the Great Barrier Reef (Lambrechts et al. 2008b) or the Scheldt River Basin (de Brye et al. 2010). Therefore, a finite-element approach is preferred over the traditional finite-difference approach, as

unstructured meshes allow to refine the computational grid in the narrow channels of the delta. In addition, as local conditions at bifurcations may play a fundamental role in discharge division, boundaries can be better represented with an increased resolution.

Calibration and validation of coastal hydrodynamic models usually rely on the correct representation of water levels and flow velocities at tidal frequencies. Although the tidal motion may account for a large amount of the variability in the dynamics of the system, it only accounts for a limited portion of the frequency domain. Studies dealing with tides and river discharge should also capture the portion of the spectrum corresponding to subtidal variations. In this context, continuous time-series of water levels are readily obtained, but particularly in large river systems, discharge measurements require a substantial effort. Repeated surveys with Acoustic Doppler Current Profilers (ADCPs) mounted on a boat are increasingly being used to understand complex flows at cross-sections in natural environments (Dinehart and Burau 2005a, b). Discharge measurements can then be obtained at a bifurcation spanning the major tidal frequencies and can be repeated at neap tide and spring tide. Several of such discharge surveys were acquired as validation data for this study.

This paper continues as follows. Section 2 introduces the Mahakam Delta channel network and measuring network. Section 3 presents discharge measurements at the principal bifurcations in the delta. Section 4 briefly

describes the implementation of SLIM to the Mahakam case. Section 5 shows the calibration and validation of the numerical model with fieldwork measurements. Section 6 investigates the effect of tides on discharge division. Finally, Section 7 presents a summary and the conclusions.

2 Field site and instrumentation

The Mahakam river is located in the East Kalimantan province, Indonesia (Fig. 1). The catchment area is approximately 75,000 km² and the total river length is about 900 km, of which three quarters are navigable. The annual mean river discharge has been estimated in the order of 3000 m³s⁻¹ (Allen and Chambers 1998). East Kalimantan province is characterized by a tropical rain forest climate with a dry (May to September) and a wet (October to April) season, governed by the Monsoons. The river mouth is separated from the upper reaches of the catchment by an alluvial plain located about 150 km upstream. During periods of heavy rainfall, strong floods up to 5000 m³s⁻¹ can rise the mean water level more than 5 m. A system of interconnected lakes with a total area of about 400 km² creates a buffer capacity damping flood surges and resulting in a relatively constant discharge in the lower reaches of the river.

At the delta apex (DA), the Mahakam river drains into a regular fan-shaped delta composed of a

Fig. 1 Location map of the Mahakam River in East Kalimantan, Indonesia. *Black dots* denote H-ADCP discharge stations, separated by about 300 km

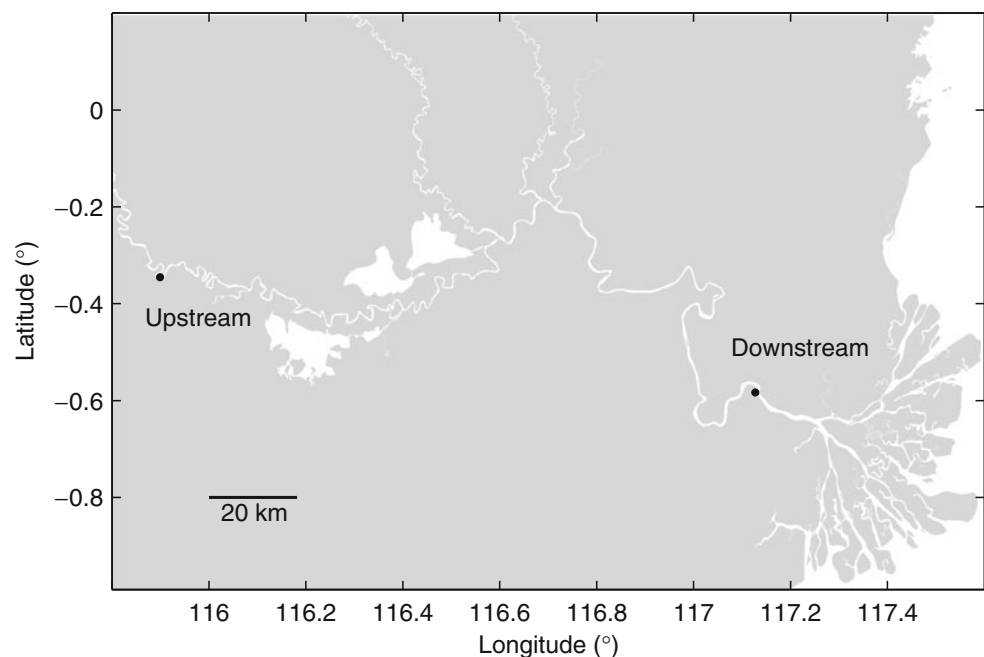


Table 1 Overview of main tidal constituents, obtained from a harmonic analysis of water levels gauged at an outlet in the northern part of the delta

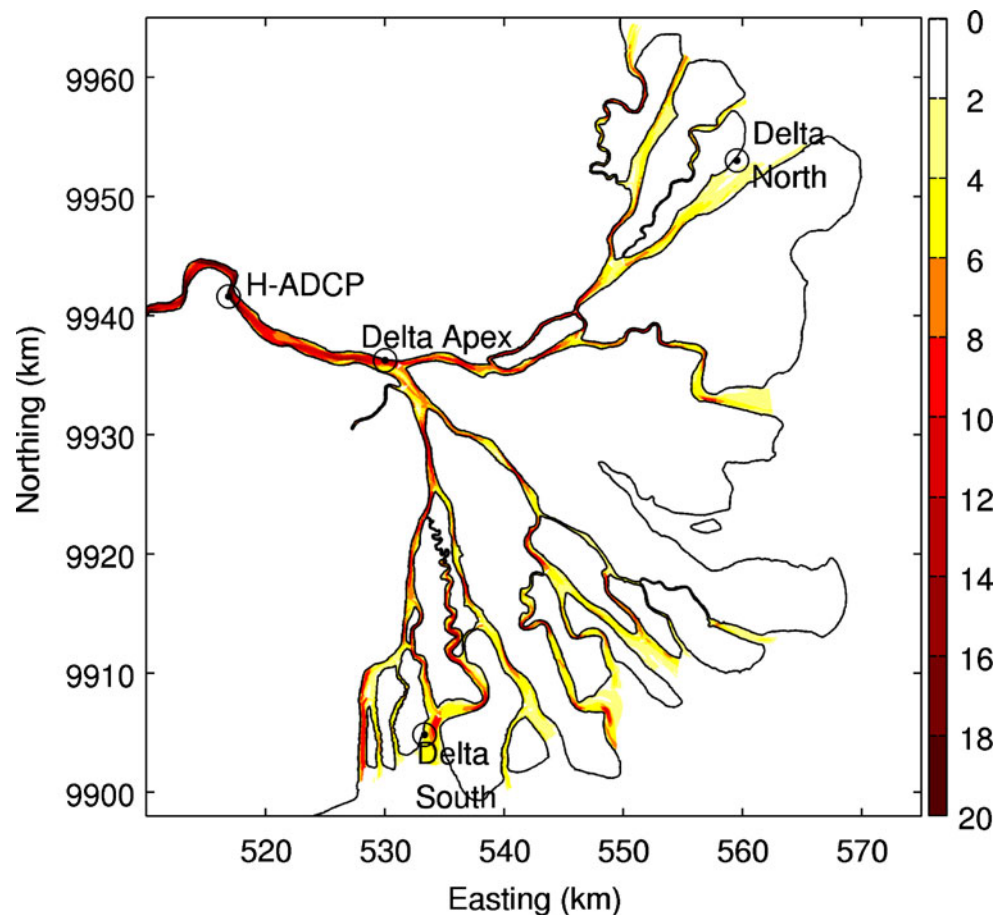
Constituent	Amplitude (cm)	Phase (°)
Q1	4	263.07
O1	19	254.36
P1	7	315.38
K1	24	256.01
N2	7	165.44
M2	55	146.69
S2	40	263.30
K2	15	354.23

quasi-symmetric network of rectilinear distributaries and sinuous tidal channels. The Mahakam delta encompasses two fluvial distributary systems directed SE and NE, comprising eight and four outlets debouching into the sea, respectively. The inter-distributary zone is tide-dominated and allocates many tidal channels, which are only occasionally connected to the fluvial system. Salinity intrusion generally reaches to about 10 km seaward from the DA (or 30 km landward from the coast). Only

during extremely low flows, such as the El Niño-related drought in 1997, salinity intrusion can reach beyond the DA. The study area is therefore generally subject to freshwater conditions. Due to the mild slope of the river, the tidal wave can propagate up to 190 km from the river mouth, depending on the river discharge.

A measuring network was setup along the lower 400 km of the river, for a period of about 18 months. It consisted of several water level gauges distributed along the river and in the delta. Two horizontally deployed Acoustic Doppler Current Profilers (H-ADCPs) were installed upstream of the lakes region, and near the DA (see Fig. 1). The measuring protocol of the water level gauges was set to yield a 1-min average every 15 min while that of the H-ADCPs was set to yield a 10-min average every 30 min. Both instruments recording at 1 Hz. Table 1 displays amplitudes and phases of the main tidal constituents obtained from a harmonic analysis of surface elevation, measured at an outlet in the northern part of the delta. Velocity measured with the H-ADCP was converted to river discharge using conventional shipborne ADCP discharge

Fig. 2 Bathymetry (in meters below mean sea level) of the Mahakam Delta channel network. Easting and Northing coordinates correspond to UTM50M. Depths are in meters below mean sea level. The discharge station, indicated by H-ADCP, is located upstream of the DA. Water level stations are located just before the DA and at the seaside of the northern and southern distributaries



measurements. At the downstream discharge station, where tides dominate, seven 13-h ADCP campaigns were carried out spanning high- and low- flow conditions, during spring tide and neap tide. Upstream of the lakes, where the tidal influence is negligible, eight 6-h ADCP campaigns also covered a wide range of flow conditions. Details of the procedures to convert flow velocity across the river section into water discharge can be found in Sassi et al. (2011), who present an adaptation to the method described in Hoitink et al. (2009).

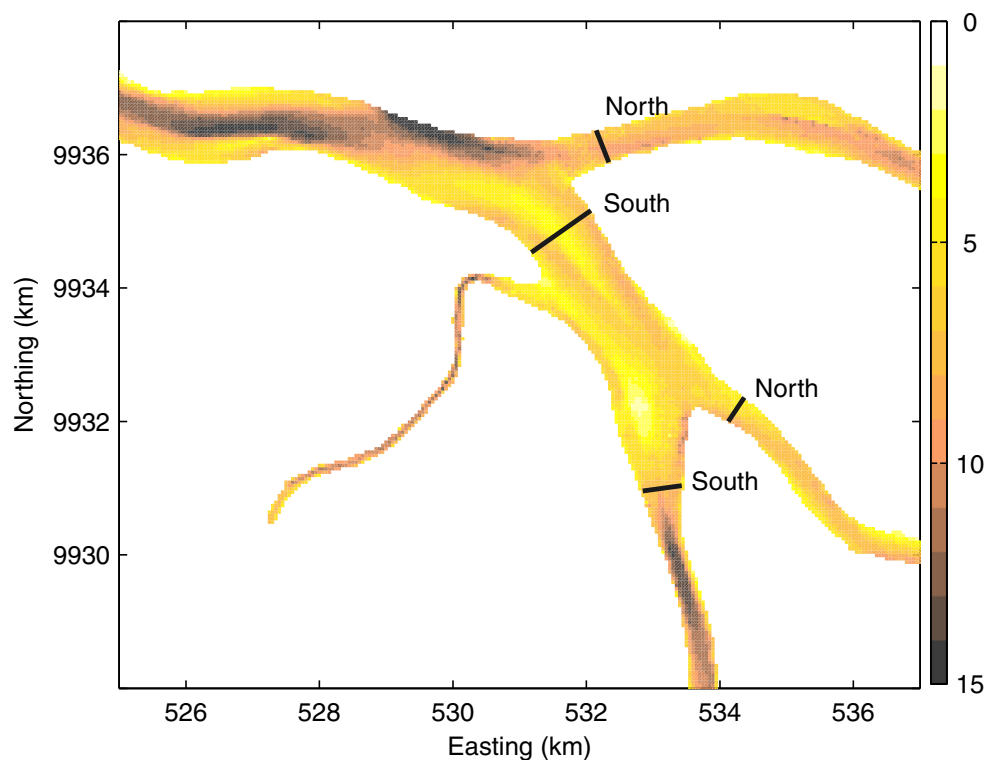
An intensive bathymetric survey with a single-beam echosounder was conducted covering the main part of the river, its tributaries, the three lakes and the delta region. Transect data of bed elevation were projected on a curvilinear grid based on linear interpolation (Legleiter and Kyriakidis 2007) to produce the bathymetric map of the channels. Figure 2 shows the bathymetry of the delta, which has been simplified by omitting tidal channels not connected to the fluvial network. All channels in the delta have variable depth, generally ranging between 5 and 15 m. The distributaries become shallower seawards; the river is consistently deeper, with an average depth of 15 m. Noteworthy are several deep spots usually located at bends, junctions and constrictions.

3 Surveys to establish discharge distribution

Discharge measurements were carried out at the principal bifurcating branches in the delta (Fig. 3). The bathymetry of the river, upstream of the DA, features a meandering thalweg which continues through the northern branch. At the southern branch, an elongated depositional area in the middle of the channel, extending about 4 km, divides the channel in two well-defined water courses. The southernmost of these water courses cuts through the elongated bank, leading to the northern branch of the first bifurcation. It is interesting to note the shallow area at the confluence of a small tributary and the southern branch, which defines another water course leading to the southern branch of the Bif.

With a boat-mounted ADCP, 13-h transects were navigated to collect velocity profiles at the two principal bifurcations of the delta, hereinafter DA and Bif. Navigated transects during spring tide and neap tide covered the same path. The research boat was equipped with a 1.2 MHz RDI Broadband ADCP measuring in mode 12, a multi-antenna Global Positioning System compass operating in differential mode (D-GPS) and a single-beam echo-sounder. The ADCP measured a single ping ensemble at approximately 1 Hz with a depth cell size

Fig. 3 Bathymetry (in meters below mean sea level) of the DA and the Bif. *Black lines* indicate the cross-river transects navigated to obtain discharge estimates in the northern and southern channels of the two principal bifurcations



of 0.35 m. Each ping was composed of six sub-pings separated by 0.04 s. The range to the first cell center was 0.86 m from the surface. The boat speed ranged between 1 and 3 ms^{-1} . To compute flow velocity with respect to a fixed reference frame, the boat speed vector was subtracted from the measured velocity vector. Boat speed was computed for each ensemble using Bottom Tracking (BT) and the D-GPS compass system. BT-derived boat speed estimates are known to be biased by sediment transport during strong currents, because the moving bed creates an apparent velocity in the same direction as the flow (Rennie et al. 2002). Therefore, when available, we corrected flow velocity with the D-GPS compass system.

Each ADCP ensemble represents a vertical profile of the three flow velocity components. A transect can be defined as the path in between two opposing riverbanks. Within a transect and within the measuring range of the ADCP, discharge was computed as (Simpson 2001)

$$Q(t) = \int_0^T \int_0^H (\mathbf{v}_S \times \mathbf{v}_F) \cdot \hat{k} dz dt \quad (1)$$

where Q is water discharge ($\text{m}^3 \text{s}^{-1}$), t is time, \mathbf{v}_S is boat velocity vector as determined with the BT or D-GPS systems (ms^{-1}), \mathbf{v}_F is water velocity vector from each ADCP ensemble (ms^{-1}), \hat{k} is a unit vector in the

vertical direction, dz is vertical differential depth, t' is time within a transect during which Q is assumed independent of T , H is total water depth (m), and T is total transect time (s). T is typically about 5 min for a channel width of 500 m. The integrand can be written as

$$X = (\mathbf{v}_S \times \mathbf{v}_F) \cdot \hat{k} = v_{Fx}v_{Sy} - v_{Sx}v_{Fy} \quad (2)$$

where X has units of discharge per unit width per unit time, and x and y are the two horizontal coordinates. Discharge near the bottom and near the surface was estimated by computing the slope of the three uppermost valid bins to extrapolate X up to the surface, and by fitting a constant power law to the 20% lowermost valid bins to extrapolate X down to the bottom. Discharge near the banks was obtained by linearly extrapolating X to zero at the banks.

ADCP campaigns took place during spring tide and neap tide, at both locations during the rising limb of a discharge wave. Figure 4 shows time-series of measured discharge over a semidiurnal tidal cycle, obtained at the bifurcating branches of DA (top) and Bif (bottom) during neap (left) and spring tide (right). Discharge fluctuates due to the modulation effect of the tides, which is stronger during spring tide than during neap tide. Intratidal discharge fluctuations are particularly asymmetrical during spring tides, with a long-lasting

Fig. 4 Measured discharge obtained at bifurcating branches in DA (top) and Bif (bottom) over neap (left) and spring (right) tidal conditions. Positive discharges correspond to a seaward flow direction. Solid lines smooth out temporal variations in discharge below 1.5 h

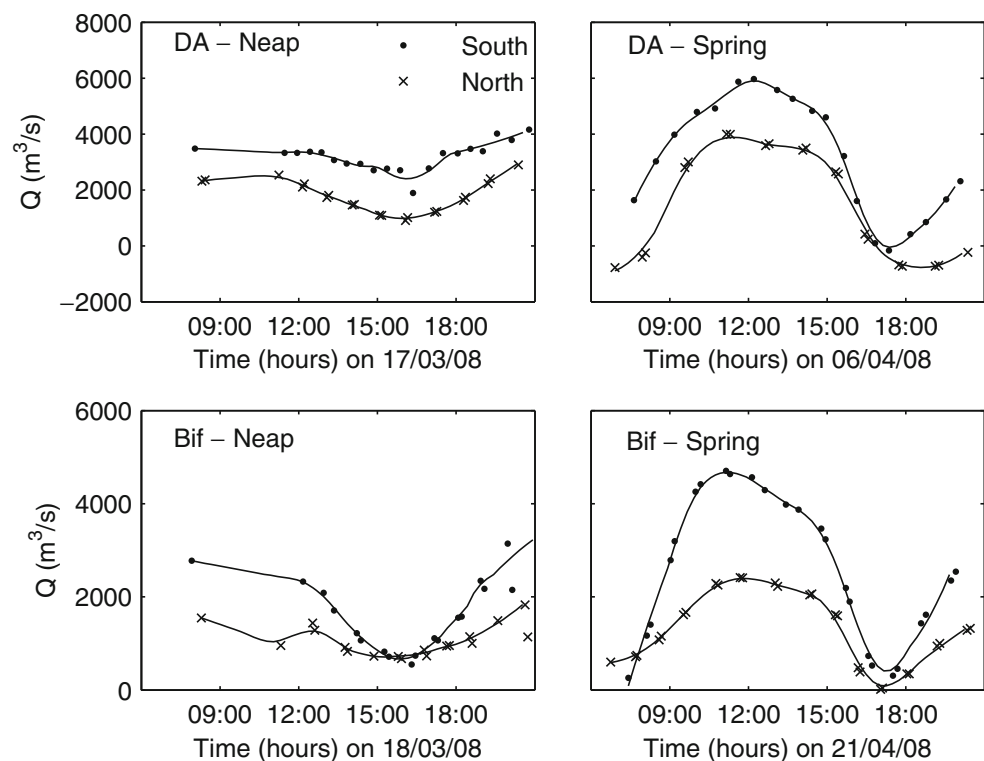


Table 2 Summary of tidally averaged quantities during the hydrographic campaigns, Delta Apex (DA) and First Bifurcation (Bif)

Location	Date	Tide	Branch	W (m)	A (m ²)	Q (m ³ s ⁻¹)
DA	17-Mar-2008	Neap	North	530	4080	1920
			South	910	5980	3480
DA	06-Apr-2008	Spring	North	500	3960	1430
			South	1010	6580	3240
Bif	18-Mar-2008	Neap	North	400	2650	1150
			South	600	4720	2140
Bif	21-Apr-2008	Spring	North	450	3080	1330
			South	750	5470	2650

ebb and comparatively shorter flood. At the northern branch at DA, during spring tides, the flood period leads to a landward flow for approximately 30% of the tidal cycle. It is interesting to note that this does not occur at the northern branch of Bif, despite that this junction is closer to the sea.

A synoptic overview of the tidally averaged quantities summarizing the moving-boat ADCP campaigns is presented in Table 2. The combined North and South discharge at Bif may be expected to be similar to the discharge measured at the southern branch of DA. Regarding neap tide, the difference is indeed merely 6%. During spring tide, the difference reaches 20%, but the spring tide measurements at DA were taken 2 weeks earlier than the ones at Bif. Besides measurement errors, there are three other reasons why the discharge averaged over a semidiurnal tidal cycle is not necessarily identical for successive spring-neap cycles. First of all, the river discharge changes significantly in 2 weeks time (see Fig. 6). Secondly, with a 13-h measurement series, diurnal tides cannot be properly isolated from the subtidal discharge. Diurnal tides feature a spring-neap cycle synchronized with the 27.32-day orbital cycle of the Moon (Kvale 2006; Hoitink 2008), which has a slightly different period than the familiar spring-neap cycles induced by the 29.52-day cycle of lunar phases. Finally, the difference can partly be caused by the small tributary debouching in between DA and Bif.

4 Numerical model

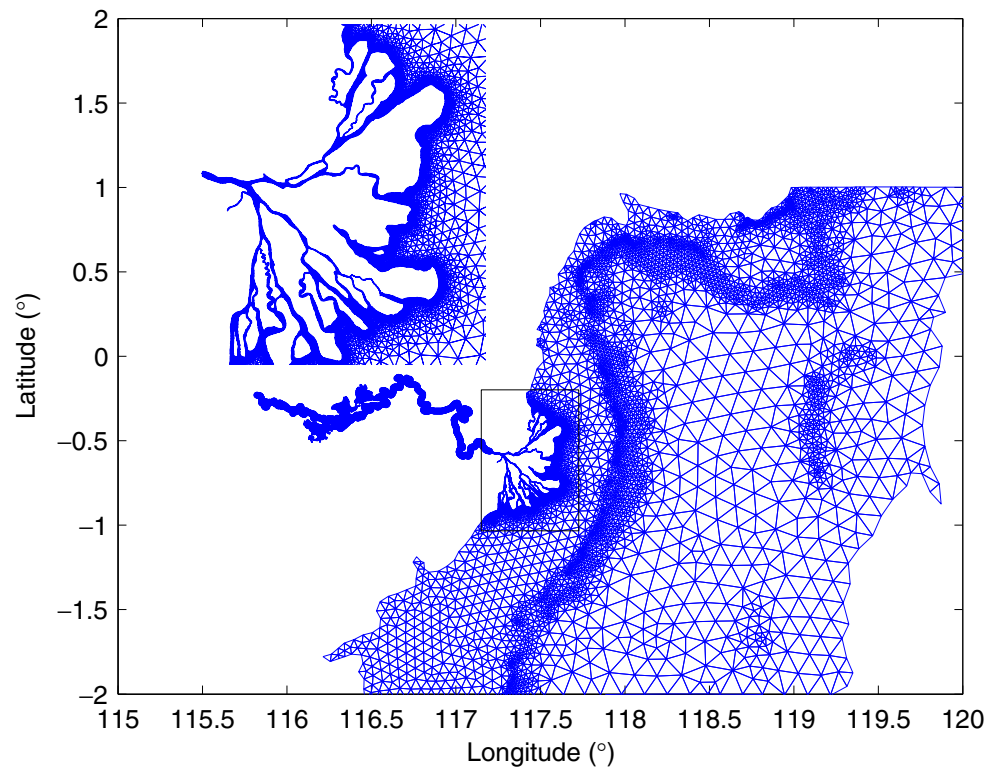
A depth-averaged version of SLIM was used. Two 2D computational domains were defined to cover the Mahakam delta and the lakes, which were connected to a 1D representation of the river and parts of its tributaries. Bathymetry was obtained from measurements in all domains, except for the outer delta and continental shelf, where GEBCO (www.gebco.net) database information was used. Figure 5 shows the computational mesh of the numerical model. Over 70% of

the elements represent the delta. Details of the model implementation can be found in de Brye et al. (2011).

The model was forced with tides from the global ocean tidal model TPX07.1 at open boundaries located far away from the delta, stretching over the entire Makassar Strait (Fig. 5). The 2D shallow-water equations succeed in representing the propagation of the tides through the strait and onto the continental shelf, up to the outlets of the delta. Although strong wind conditions may hamper the 2D approach, the impact of wind in the Makassar Strait is limited. Baroclinic effects associated to 3D flows were assumed to have negligible interaction with the delta.

At the upstream boundary, the model was forced with a discharge series derived from H-ADCP measurements. At the tributaries connected to downstream modeling domain, discharge series were obtained from a rainfall-runoff model, calibrated with the measured discharge series of the principal subcatchment (Fig. 6). The slope of the river was set to 1×10^{-5} . This value was inferred from an analysis of the subtidal momentum balance following Buschman et al. (2009), using flow measurements from the H-ADCP near Samarinda and surface elevation from the level gauge at DA. Bottom friction, represented by a Manning coefficient n , was obtained from the following calibration procedure, in which the computational domain is split in three parts. A constant Manning coefficient ($n = 0.023$) was assumed in the deepest part of the domain beyond the slope break of the continental shelf, since it was found to be a good choice for the continental shelf in another application of the SLIM model (de Brye et al. 2010). A different constant Manning coefficient represented bottom roughness in the fluvial part of the domain, upstream of the mouths of the distributaries. In the continental shelf part in between the latter two regions of constant bottom roughness, a linear transition between the deep water part of the model and the distributaries was assumed. We have varied the Manning coefficient in the inner region from 0.017 to 0.029 and we have tested five cases, of which $n = 0.026$ in the inner region resulted in the best match with our

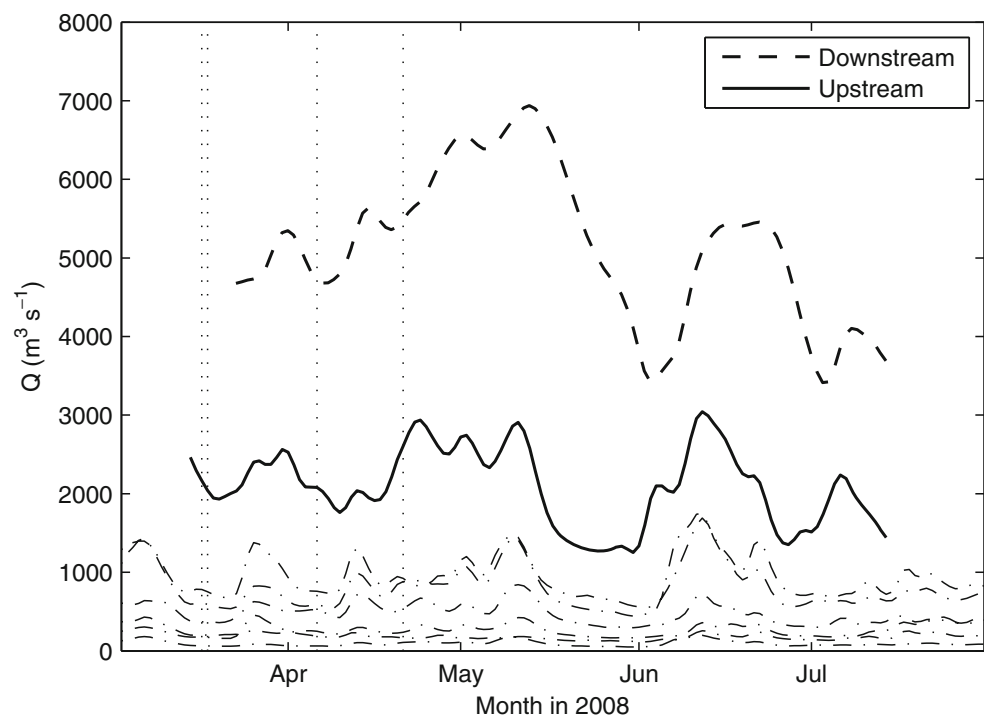
Fig. 5 Mesh of the computational domain. The 2D domain is connected to a 1D river and tributaries network



measurements. Those test cases were simulated over a time-span of 2 weeks. The numerical simulations for calibration of the model were carried out with water levels obtained at the three stations depicted in Fig. 2,

and discharge estimates from the monitoring station located in Samarinda (Sassi et al. 2011). The calibration presented herein is slightly different from a previous approach described by de Brye et al. (2011), who

Fig. 6 Measured discharge series at upstream and downstream locations. *Dash-dotted lines* indicate discharge series in the tributaries as obtained from the rainfall-runoff model. *Dotted lines* denote the date of discharge measurements at the bifurcations



calibrated the model with water levels only. The following section presents the results of simulations with the optimized bottom roughness configuration. Model runs spanned from March through April 2008.

5 Results

Time-series of water levels from the model and the observations were subjected to a Continuous Wavelet Transform, using a Morlet mother wavelet. Wavelet analysis was preferred over traditional harmonic analysis because of its ability to deal with non-stationary signals (Jay 1997). The scale resolution used in the wavelet transform allowed us to distinguish between main tidal species, instead of between tidal constituents. The wavelet spectrograms yielded amplitudes of quarterdiurnal (D_4), semidiurnal (D_2) and diurnal (D_1) fluctuations. Time-series of water levels and discharge were averaged over a 24-h period to obtain subtidal water levels and discharges (respectively).

Spectrograms generally show a well-defined gap between the tidal band, where the main tidal species occur, and the subtidal band, where river discharge fluctuations and associated interactions with the tidal motion dominate (see Fig. 7). The frequencies at which wavelet power is resolved is an array of powers of 2, which is chosen such that D_1 , D_2 and D_4 are resolved (Buschman et al. 2009). With that choice, it is not possible to sharply distinguish between fortnightly fluctuations and monthly or seasonal fluctuations. Nevertheless, we isolated the fortnightly variation by delimiting

the fortnightly frequency domain in the normalized global wavelet power spectrum. This procedure yields fortnightly power concentrated in a band corresponding roughly to 10–20 days. Fortnightly amplitudes of water levels obtained accordingly are denoted by $D_{1/14}$. It is noted that, to some degree, power from adjacent regions in the spectrogram, such as that associated to weekly and monthly fluctuations, may have leaked into the selected window.

5.1 Validation of modeled water levels and flow

Figure 8 shows time-series of subtidal water level and amplitudes of D_4 , D_2 , D_1 and $D_{1/14}$ from observations at Delta North, and corresponding model results after calibration. Diurnal and semidiurnal amplitudes show a fortnightly periodicity associated with the tropical and synodic spring-neap cycles, i.e. 13.6 and 14.8 days, respectively. Quarter diurnal amplitudes covary with semidiurnal amplitudes, indicating that most of the variation in D_4 is driven by nonlinear interaction of D_2 with itself. Variations in $D_{1/14}$ are the result of frictional forces induced by a combination of D_1 , D_2 and river flow (Godin 1999; Buschman et al. 2009).

At Delta North, a good agreement between the model and observations is obtained for the D_1 and D_2 tidal species (Fig. 8). Amplitudes of $D_{1/14}$ are underestimated, but are not important for the overall dynamics at this location. Amplitudes of D_4 are well represented, although some underestimation can be observed. The latter discrepancy can partly be explained by the idealization of the coastlines and riverbanks, which have

Fig. 7 Wavelet spectrogram (left) and normalized global wavelet power spectrum (right) for water level time series at DA station

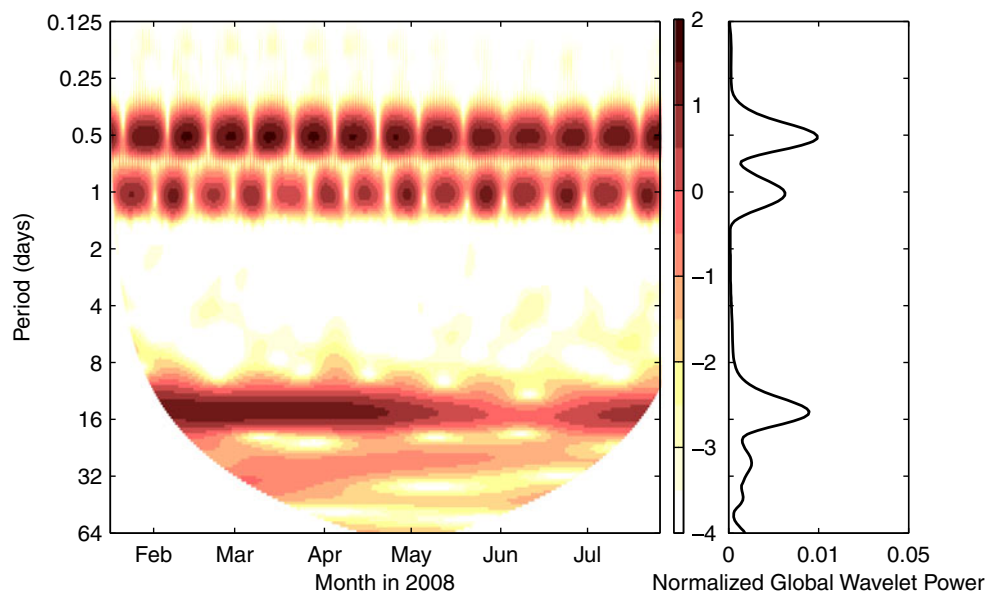
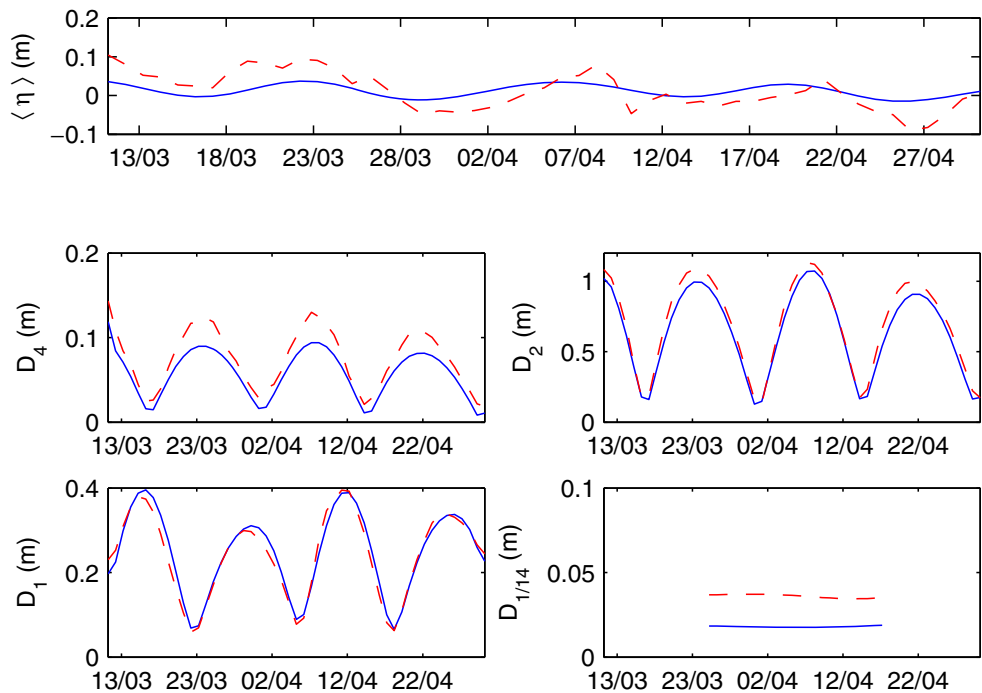


Fig. 8 Subtidal water level $\langle \eta \rangle$ and water level amplitude obtained from a wavelet decomposition, isolating the three main tidal species (D_1 , D_2 and D_4) and the fortnightly amplitude $D_{1/14}$ from observations at the Delta North station (red dashed line), and from the corresponding model results (blue solid line)



a significant control over the nonlinear terms in the equations of motion. At Delta South, the agreement between the model and observations is high both for the main tidal species and for the fortnightly amplitude (Fig. 9). We expect water levels in Delta South to be better represented than in Delta North, because the

bathymetry of the southern distributary system shows deeper channels than in the northern one. Shallower sections are likely to amplify water levels, if the bathymetry or the model geometry are inaccurate. Other reasons may be the accuracy of GEBCO database in shallow areas, especially in the vicinity of the outlets.

Fig. 9 Subtidal water level $\langle \eta \rangle$ and water level amplitude obtained from a wavelet decomposition, isolating the three main tidal species (D_1 , D_2 and D_4) and the fortnightly amplitude $D_{1/14}$ from observations at the Delta South station (red dashed line), and from the corresponding model results (blue solid line)

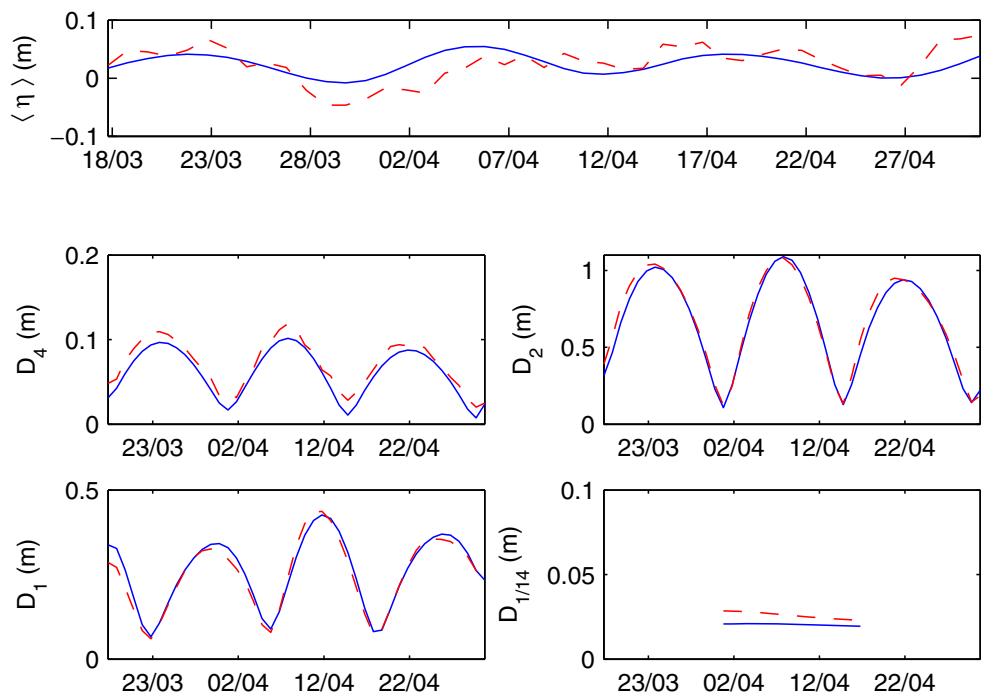


Fig. 10 Subtidal water level $\langle \eta \rangle$ and water level amplitude obtained from a wavelet decomposition, isolating the three main tidal species (D_1 , D_2 and D_4) and the fortnightly amplitude $D_{1/14}$ from observations at the DA station (red dashed line), and from the corresponding model results (blue solid line)

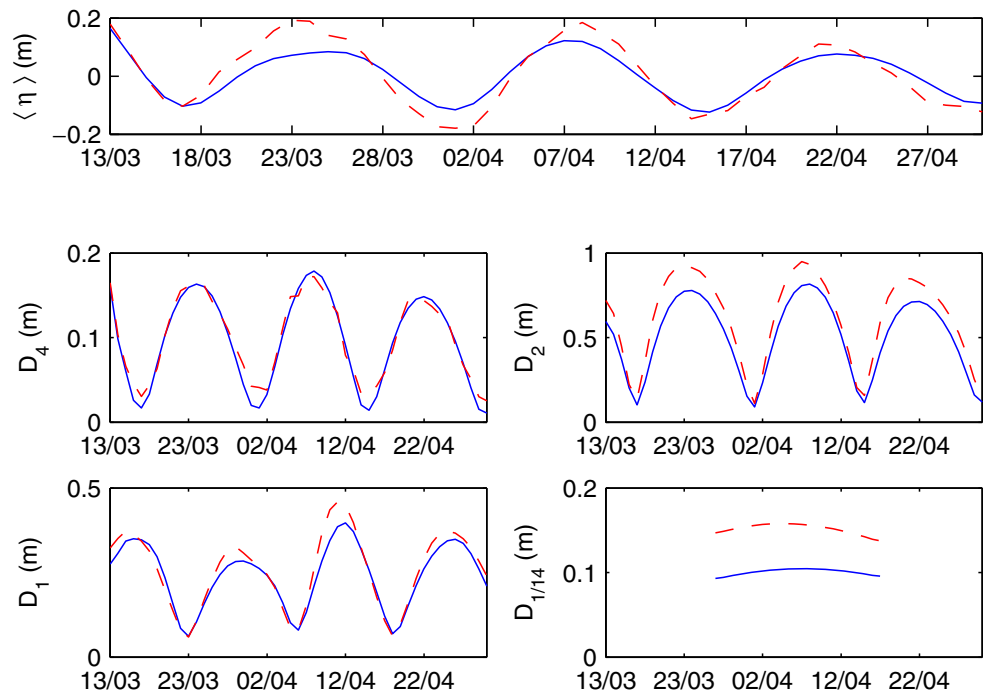


Figure 10 shows the comparison between model and observation at DA, located approximately 40 km from the outlets. At this location tidal waves have undergone transformations while propagating through the main branches of the delta. Amplitudes of D_1 and D_2 are here slightly underestimated, whereas D_4 is well rep-

resented. Amplitudes of $D_{1/14}$ are larger than in coastal locations, increasing upriver to a point where tides are significantly damped by the river discharge (LeBlond 1979; Godin 1999; Buschman et al. 2009). Disagreement of diurnal and semidiurnal species are likely related to the exclusion of tidal channels.

Fig. 11 Subtidal flow velocity $\langle U \rangle$ and velocity amplitude obtained from a wavelet decomposition, isolating the three main tidal species (U_1 , U_2 and U_4) and the fortnightly amplitude $U_{1/14}$ from observations at the H-ADCP discharge station (red dashed line), and from the corresponding model results (blue solid line)

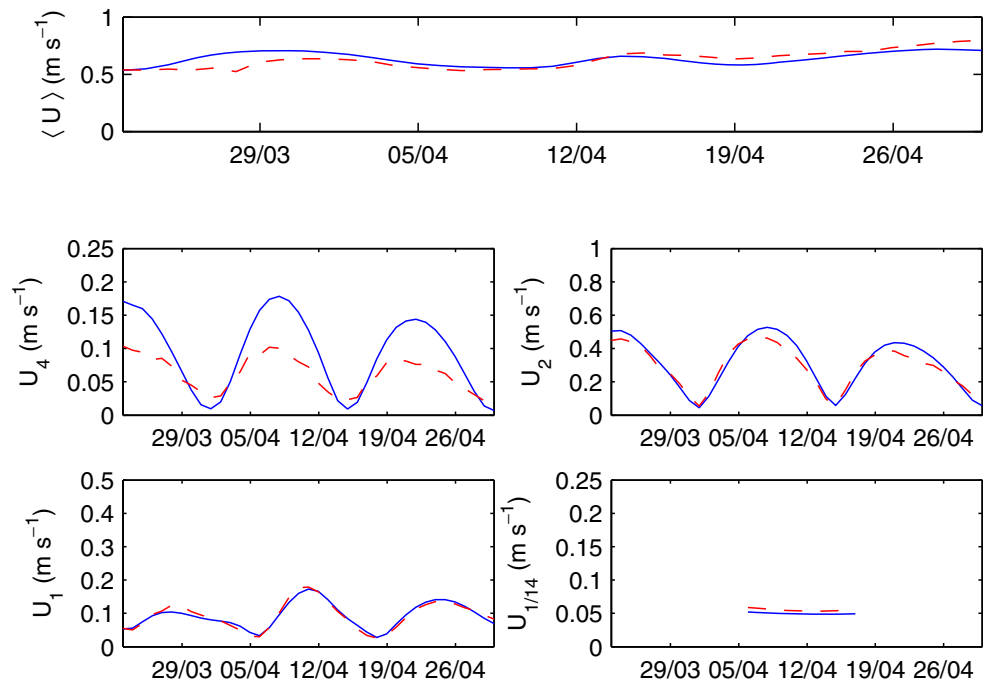
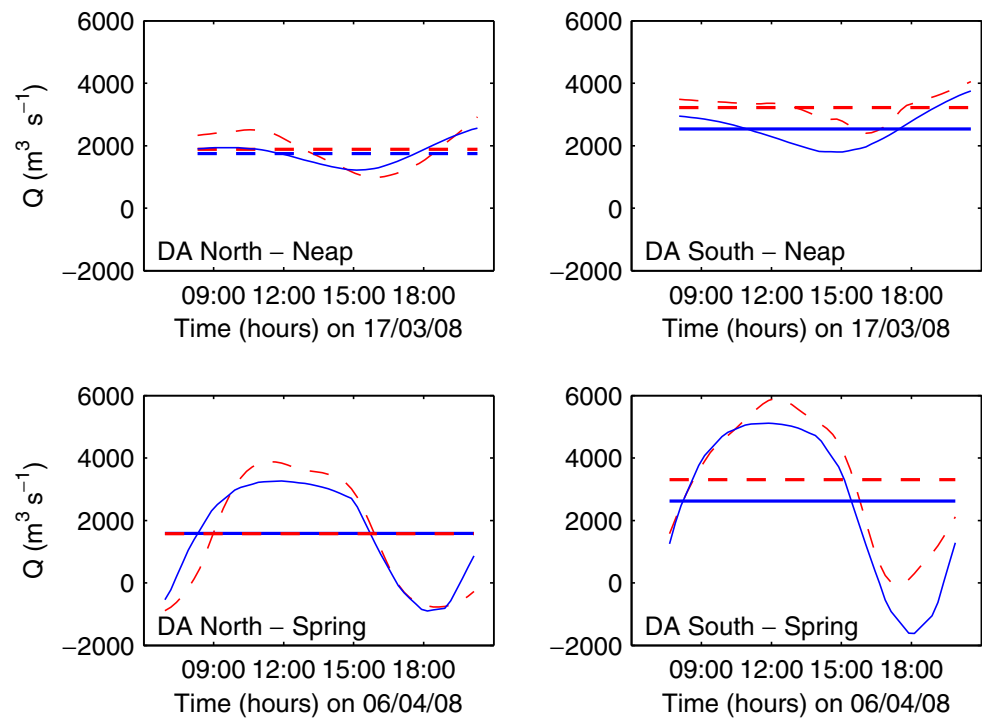


Fig. 12 Time-series of water discharge from model results (blue solid line) and observations (red dashed line) at the northern (left) and southern (right) branches during neap tide (top) and spring tide (bottom) at DA station. Positive discharge coincides with seaward flow



Time series of mean flow velocity obtained from the downstream H-ADCP discharge station was also subjected to the wavelet analysis previously described. Figure 11 compares model and observations at the H-ADCP discharge station. The agreement for the U_1 , U_2

and $U_{1/14}$ tidal species is high. The fortnightly amplitudes of flow velocity are significant, exceeding 0.05 ms^{-1} . The model overestimates the quarter-diurnal flow variation, which may be related to spatial variations in bed roughness that were not accounted for.

Fig. 13 Time series of water discharge from model results (blue solid line) and observations (red dashed line) at the northern (left) and southern (right) branches during neap tide (top) and spring tide (bottom) at Bif station. Positive discharge coincides with seaward flow

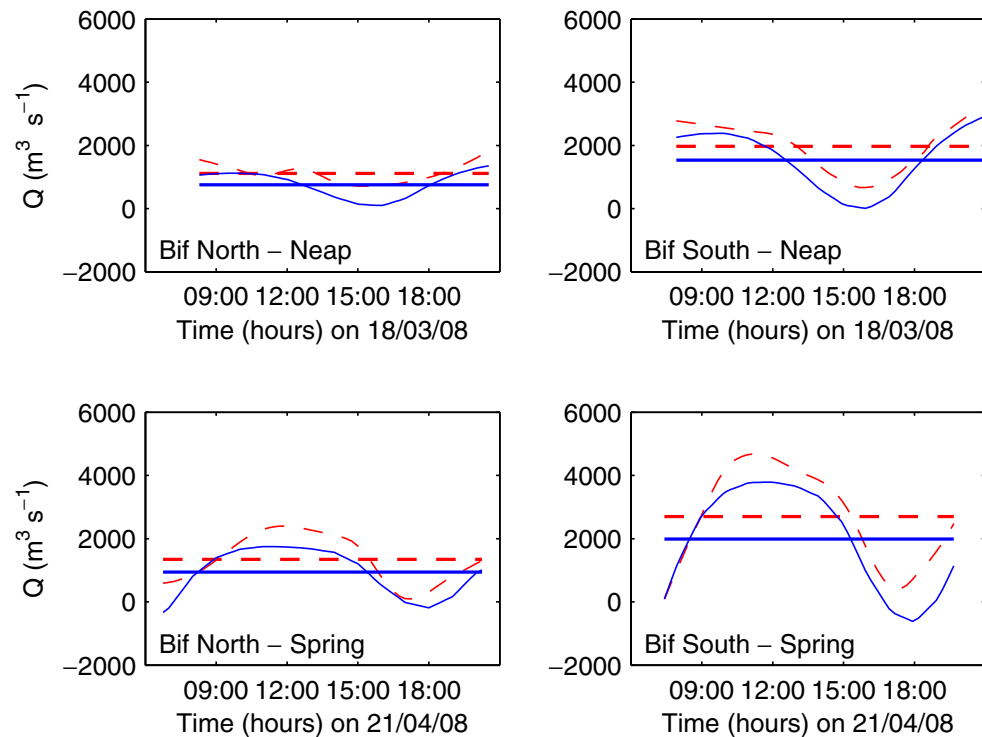
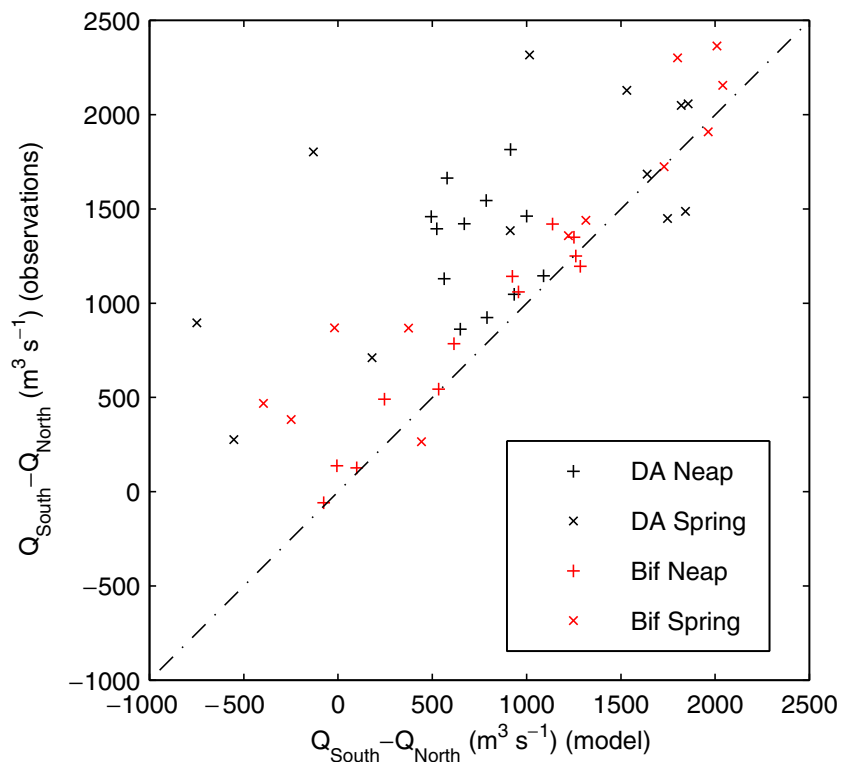


Fig. 14 Discharge difference between branches obtained with the model and with observations



5.2 Validation of modeled discharge division

To validate the numerical model, we compare model results with measured discharges at DA and Bif stations. Figure 12 shows the discharges in the northern (left) and southern (right) branches of DA station during neap tide (top) and spring tide (bottom), both for model results and for the observations. The model correctly represents the observed intra-tidal discharge variation in both bifurcations during spring tide and neap tide conditions. During spring tides in the southern branch, model results show a landward flow which is not present in the observations. The difference in tidally averaged discharge between model and observation in the northern branch is negligible, both during spring tide and during neap tide. The model underestimates the subtidal discharge in the southern branch by roughly $500 \text{ m}^3 \text{ s}^{-1}$ (approximately 15%), in both tidal periods considered. Figure 13 compares discharge from the model and the observations at Bif station, showing that differences in subtidal discharge are within 10%. Figure 14 investigates the variation in discharge division over the downstream branches both at DA and Bif stations. To some extent, the discharge division in the model is too asymmetrical, especially at DA station during spring tide.

We attribute the minor discrepancies between model results and observations to the limited degree in which

spatial variations of bed roughness are accounted for. Differences in bed roughness between distributaries may be explained by sediment sorting at the apex (Frings and Kleinhans 2008), which leads to variation in bed material and in the occurrence of bed forms. Other possible causes of discrepancies are the representation of the river banks in the model, which does not capture the geometric complexity of lateral channels, and the limited number of tidal constituents used to force the model.

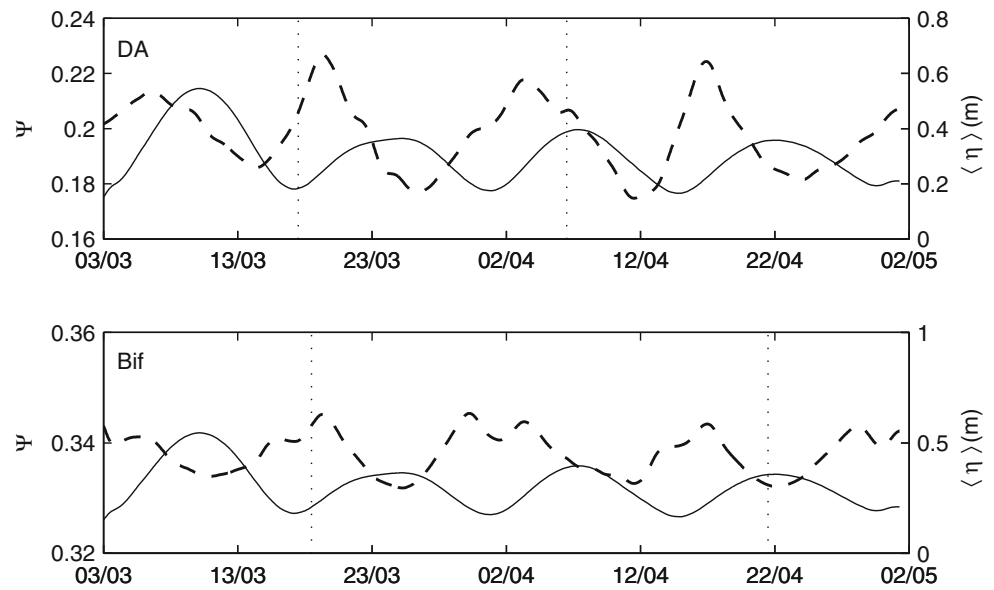
6 Subtidal discharge division

The subtidal discharge division at a bifurcation is here quantified as (Buschman et al. 2010)

$$\Psi = \frac{\langle Q_1 \rangle - \langle Q_2 \rangle}{\langle Q_1 \rangle + \langle Q_2 \rangle} \quad (3)$$

where brackets indicate tidal average, and suffixes 1 and 2 stand for the southern and northern branches, respectively. The discharge asymmetry index (Ψ) is zero for an equal discharge division; it is positive when subtidal discharge in the southern channel is larger, attaining a value of one when all subtidal discharge is carried by the southern channel, and minus one for the reverse case. Figure 15 shows Ψ and subtidal water level $\langle \eta \rangle$ for DA and Bif stations, obtained from the model.

Fig. 15 Discharge asymmetry index Ψ (dashed line) and subtidal water level $\langle \eta \rangle$ (solid line) as a function of time at DA (top) and Bif (bottom). Dotted lines denote the date of discharge measurements at the bifurcations



The subtidal water level variation features a spring-neap oscillation directly in response to the strength of the forcing. The subtidal discharge division covaries with subtidal water level, although it lags behind the spring-neap cycle, and peaks at the transition between neap tide and spring tide. The discharge division at both bifurcations is particularly asymmetrical at the onset of spring tide, tending to be more equally distributed at the peak of spring tides.

To distinguish between effects of tides, river discharge and river-tide interactions on subtidal discharge division, subtidal discharges were decomposed using the method of factor separation (Stein and Alpert 1993). The model was run for three forcing conditions:

- Tides only: the model is forced with tides at the downstream boundary, whereas a radiative boundary condition is imposed at a suitable upstream location.
- River discharge only: the model is forced with river discharge at the upstream boundary and set to equilibrium water level at the marine boundary.
- Tides and river discharge: the model is configured as described in Section 4.

Noting that neither for tidal nor river discharge forcing $\langle Q_1 \rangle + \langle Q_2 \rangle$ is zero (Buschman et al. 2010), the subtidal discharge forced by both river flow and tides ($\langle Q \rangle$) can be decomposed as

$$\langle Q \rangle = Q_r + \langle Q_t \rangle + \langle Q_{rt} \rangle \quad (4)$$

where Q_r denotes the contribution solely due to river flow, Q_t is the contribution due to tides alone and Q_{rt} is the contribution due to river-tide interaction.

6.1 Response to tidal forcing only

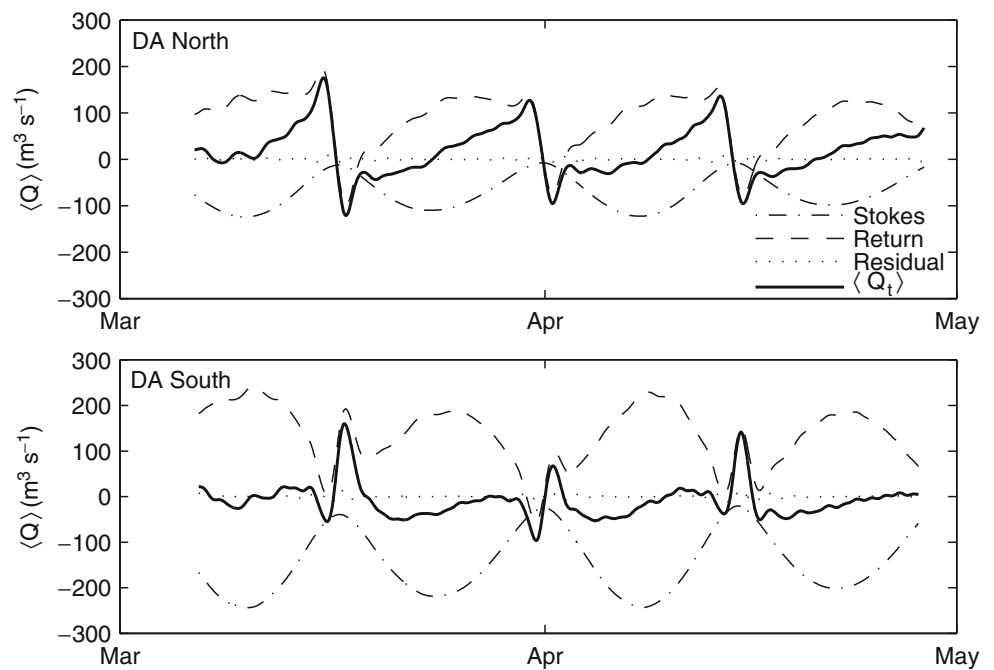
To understand the effect of tides on subtidal discharge division, the contribution from simulations forced with tides only (Q_t) is split in three components. To do so, the cross-section averaged flow velocity is decomposed according to $U = \langle U \rangle + U'$, where the prime denotes the variation during a diurnal tidal cycle. Depth can be written as $d = h + \eta$. Assuming a time-invariant channel width (W), subtidal discharge can be re-written as

$$\langle Q_t \rangle = W \langle U' \eta \rangle + Wh \langle U \rangle + W \langle U \rangle \langle \eta \rangle \quad (5)$$

where the first term denotes the Stokes transport Q_S , the second term is the return discharge Q_R and the third term is a residual term that is small as $\langle \eta \rangle$ is near-zero. In general, Q_S is directed landward, generating a water level gradient that forces a net compensating return discharge seaward. The magnitudes of Q_R and Q_S can be highly nonuniform in convergent channels, being largest close to the sea and decreasing landward. In single channels, having constant width or being convergent, the water storage is limited and Q_S and Q_R balance. Therefore, $\langle Q_t \rangle$ is small or zero. In a network channel, Q_S and Q_R do not necessarily balance, implying that $\langle Q_t \rangle$ in the bifurcating channels may have nonzero values (Buschman et al. 2010).

Figure 16 shows the decomposition of $\langle Q_t \rangle$ into contributions of the Stokes transport Q_S , return discharge Q_R and the residual term at bifurcating branches in DA station. Q_S is landward and increases during spring tides. The component due to the residual term is negligible. Values of Q_S in the southern branch are about 1.5

Fig. 16 Decomposition of subtidal discharge induced by tidal motion only ($\langle Q_t \rangle$) into contributions of the Stokes transport Q_S , return discharge Q_R and the residual term in Eq. 5, at bifurcating branches in DA station. The Stokes transport is landward whereas the return discharge is seaward



times larger than in the northern branch. In the northern branch, the net transport ($\langle Q_t \rangle$) increases toward neap tides. In the southern branch, Q_S and Q_R balance during spring tide, whereas during neap tide a transfer from the southern branch to the northern branch and back to the southern branch is observed. Then, the transfer from the northern to the southern branch takes place. When averaged over several spring-neap cycles, the net transport is nearly zero. The behavior at Bif station is similar (not shown).

The limited impact of the tides on the discharge division at DA and Bif stations relates to the large distance to the coast, which is about 40 km from the DA. The interplay between Q_S and Q_R at bifurcating branches explains the spring-neap variability in the discharge asymmetry ratio Ψ . During spring tides, Q_S and Q_R balance at each bifurcating branch, leading to an equal discharge division. During neap tides, the transfer from the southern to the northern branches driven by the Stokes flux leads to a more unequal discharge distribution, temporarily favoring the southern branch.

6.2 Tidal impact on discharge division

To carry out a systematic analysis of the causes of asymmetry in the subtidal discharge division at each of the bifurcation in the Mahakam Delta, the discharge asymmetry index Ψ (Eq. 3) was split up in three components

$$\Psi = \Psi_r + \Psi_t + \Psi_{rt} \tag{6}$$

where Ψ_r denotes the asymmetry in the discharge division from simulations with river flow, Ψ_t is obtained from the tides only simulations and Ψ_{rt} can be obtained by subtracting Ψ_r and Ψ_t from Ψ . By convention (see Eq. 3), 1 and 2 denote herein further the right and left bifurcating channel when approaching the bifurcation while moving upstream, respectively. The result of this convention is that except for the southernmost bifurcation, southerly channels have the subscript 1 and the northerly channels subscript 2.

Figure 17 shows Ψ , Ψ_r and the relative difference $(\Psi - \Psi_r)/\Psi_r$ expressed as a percentage (0–100) for each bifurcation in the Mahakam delta, computed by averaging the subtidal discharge over several spring-neap cycles. Values of Ψ range from -0.4 to 0.6 , which reflects the large variation of flow dynamics at bifurcations of the channel network. The relative difference indicates the tidal impact on subtidal discharge distribution, as it increases with the contributions from tides and river-tide interaction. Within 10 to 15 km from DA station, the tidal impact on river discharge division is within 10% in all bifurcations. Tidal impact increases seaward with a maximum value of the order of 30%. It is interesting to note that in general, the effect of tides is to hamper the discharge division that would occur in the case without tides.

Buschman et al. (2010) found that the tidal motion favors the allocation of river discharge to shorter and deeper channels, enhancing the inequality in the discharge division over two downstream channels connected to the sea. In many instances, the results

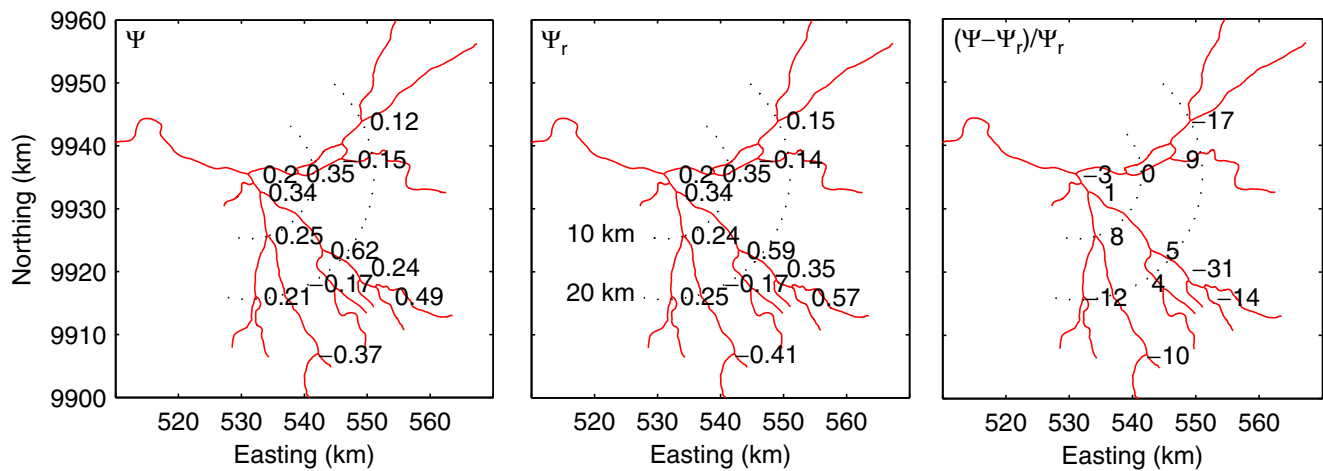


Fig. 17 Centerlines of the channels in the Mahakam delta showing the bifurcations. *Black dotted lines* indicate radial distance in km from the DA. *Numbers* indicate Ψ values at each of the bifurcations analysed. *r* stands for simulations forced with river

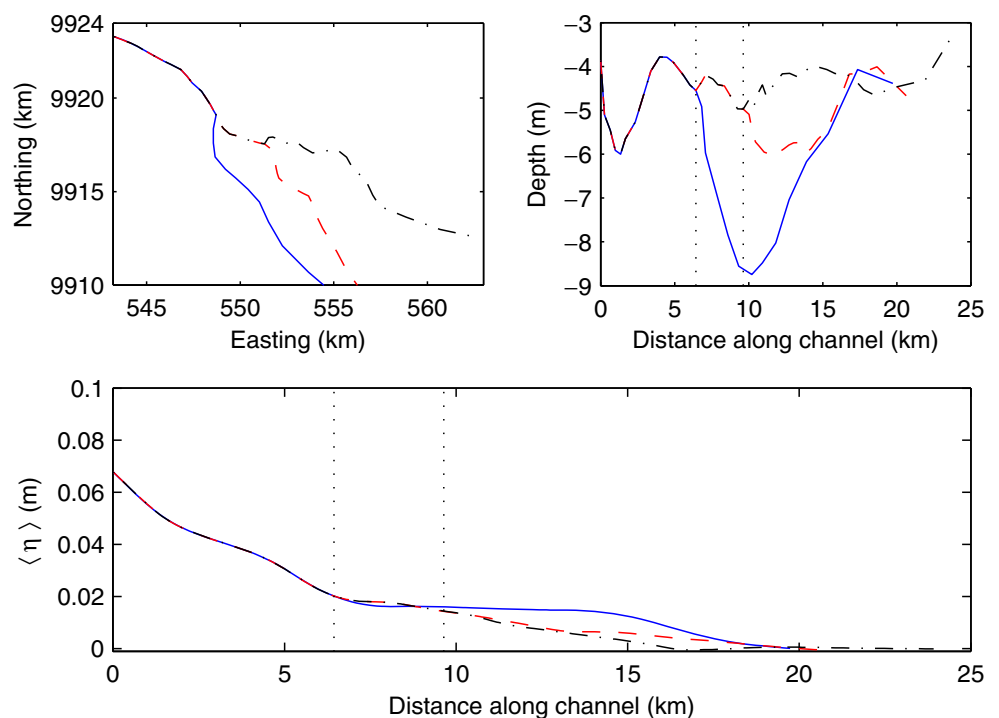
discharge only and *rt* stands for simulations forced with river discharge and tides. The relative difference is expressed as a percentage

presented herein do not confirm these findings, which suggests that simplifying the geomorphological complexity as performed by Buschman et al. (2010) may change the subtle processes governing the tidal-averaged distribution of discharge over distributaries. In the Mahakam Delta, the channels feature a very distinct bed morphology and the junction angles of the bifurcations show a large variability. In the study by Buschman et al. (2010), both downstream channels diverged with the same angle from the upstream channel. Besides the issue of geomorphological complexity,

processes occurring at a single nodal point cannot be readily translated to a network in which nodes and branches interact, which may result in chaotic behavior.

At the bifurcation that is most markedly in contrast with the results by Buschman et al. (2010), tides modify the discharge distribution by 31% (see Fig. 17). That junction connects a very deep and short sea-connected southern branch to a much smaller northern branch, which bifurcates once more in two equally long branches. The large tidal impact observed may relate to water level setup caused by river-tide interaction in the

Fig. 18 Subtidal water level profiles in the part of the Mahakam delta where the tidal impact on river discharge division is largest (*bottom*). The top left panel shows the geographical location and the top right panel the depth profiles along the channels



channels (Godin and Martinez 1994; Buschman et al. 2009). The southern channel conveys a larger share of the river discharge, resulting in a tendency to generate a subtidal water level setup, as shown in Fig. 18. At the junction, the subtidal water level is constrained by the subtidal water level in the northern channel, which is elevated by the river-tide interaction in the southern channel. The subtidal water level setup in the southern channel thus increases the subtidal water level gradient at the junction towards the northern channel, reducing the allocation of river discharge to the southern channel. We propose the term *differential water level setup* to describe this phenomenon, which is dominant in the seaward part of the Mahakam channel network. Differential water level setup may occur in many other channel networks in the world, where junctions connect large branches conveying both river and tidal discharges, to smaller branches where the tidal motion is dominant.

7 Summary and conclusion

A depth-averaged version of the unstructured-mesh, finite-element model SLIM has been used to simulate the hydrodynamics driven by river discharge and tides in the Mahakam delta channel network, East Kalimantan, Indonesia. The aim of the study was to establish and understand the tidal impact on river discharge division at the bifurcations in the delta. Two 2D computational domains were defined to cover the Mahakam delta and the lakes region, which were interconnected by a 1D computational domain representing the river and several tributaries. Measured bathymetry was used in all domains except for the continental shelf and Makassar Strait, where GEBCO database information was used. The model was forced with tides from the global ocean tidal model TPX07.1 at open boundaries, located far away from the delta, stretching across the entire Makassar Strait. At the upstream boundary, the model was forced with measured discharge series. At the tributaries, discharge series were obtained from a rainfall-runoff model from the main subcatchment, calibrated with the measured discharge series. The slope of the river was estimated from an analysis of the subtidal momentum balance inferred from data. Bottom friction was obtained from model calibration, decomposing the model domain in three regions. Model runs spanned from March to April 2008. Calibration was performed with water level time series, measured at three locations in the delta, and flow measurements at a discharge station located near the river mouth, both spanning the simulation period. Validation was performed by

comparing model results with discharge distribution measurements at the two principal bifurcations in the delta.

To distinguish between effects of tides, river discharge and their interaction, subtidal discharge was decomposed using a method of factor separation. Apart from the calibration and validation simulations, the model was run in two more configurations: imposing tides only and imposing river discharge only. The discharge asymmetry index Ψ , computed as the ratio between the difference in discharge between two branches to their sum, was computed for each case. Results from the simulations forced with tides only indicate that at the DA Ψ features a fortnightly oscillation, which is driven by the imbalance in the return discharges induced by the Stokes fluxes. When averaged over several spring-neap cycles, the net transport is nearly zero, revealing that in absence of a river discharge no residual circulation occurs. The discharge asymmetry index for simulations forced with river discharge and tides was then split up in three components ($\Psi = \Psi_r + \Psi_t + \Psi_{rt}$, where Ψ_r denotes the contribution solely due to river flow, Ψ_t the contribution due to tides alone and Ψ_{rt} the contribution due to river-tide interaction). Values of Ψ ranged from -0.4 to 0.6 , reflecting the geomorphological complexity of the Mahakam Delta. Maps of the relative difference $(\Psi - \Psi_r)/\Psi_r$, expressed as a percentage, showed that within 10–15 km from the DA, tides were found to alter the relative difference $(\Psi - \Psi_r)/\Psi_r$ by less than 10% at all bifurcations. Tidal impact increases seaward with a maximum value of the order of 30%. In general, the effect of tides is to hamper the discharge division that would occur in the case without tides. At the bifurcation where the tidal impact was largest, steepening of the tidal-averaged water level profile in the deepest and shortest channel by river-tide interaction enhanced the gradient in the longer and shallower channel. The enhanced subtidal waterlevel gradient favored the allocation of river discharge to the longer and shallower channel.

Acknowledgements This study is part of East Kalimantan Programme, supported by grant number WT76-268 from WOTRO Science for Global Development, a subdivision of the Netherlands Organisation for Scientific Research (NWO). E. Deleersnijder is a Research Associate with the Belgian Fund For Scientific Research (F.R.S. - FNRS). His contribution to the present study, as well as that of B. de Brye, was achieved in the Framework of ARC 10/15 - 028 (Communauté Française de Belgique). Fajar Setiawan and Unggul Handoko (Indonesian Institute of Sciences) are acknowledged for their contribution to the field campaigns. We thank Pieter Hazenberg and Johan Romeligh (Wageningen University) for the technical support. The first author thanks Frans Buschman for the constructive

criticism on the draft of this manuscript. The Associate Editor and an anonymous reviewer have helped improve the draft of this paper with constructive criticism.

References

- Allen GP, Chambers JLC (1998) Sedimentation in the modern and Miocene Mahakam delta. Indonesian Petroleum Association, Jakarta, p 236
- Bertoldi W, Tubino M (2007) River bifurcations: experimental observations on equilibrium configurations. *Water Resour Res* 43(10). doi:[10.1029/2007WR005907](https://doi.org/10.1029/2007WR005907)
- Bolla-Pitaluga M, Repetto R, Tubino M (2003) Channel bifurcation in braided rivers: equilibrium configurations and stability. *Water Resour Res* 39(3):1046. doi:[10.1029/2001WR001112](https://doi.org/10.1029/2001WR001112)
- de Brye B, de Brauwere A, Gourgue O, Krn T, Lambrechts J, Comblen R, Deleersnijder E (2010) A finite-element, multi-scale model of the Scheldt tributaries, river, estuary and ROFI. *Coast Eng* 57(9):850–863
- de Brye B, Schellen S, Sassi M, Vermeulen B, Kärnä T, Deleersnijder E, Hoitink T (2011) Preliminary results of a finite-element, multi-scale model of the mahakam delta (Indonesia). *Ocean Dyn* 1–14 (in press). doi:[10.1007/s10236-011-0410-y](https://doi.org/10.1007/s10236-011-0410-y)
- Buijsman MC, Ridderinkhof H (2007) Water transport at subtidal frequencies in the Marsdiep inlet. *J Sea Res* 58(4):255–268
- Buschman FA, Hoitink AJF, Van Der Vegt M, Hoekstra P (2009) Subtidal water level variation controlled by river flow and tides. *Water Resour Res* 45(10). doi:[10.1029/2009WR008167](https://doi.org/10.1029/2009WR008167)
- Buschman FA, Hoitink AJF, Van Der Vegt M, Hoekstra P (2010) Subtidal flow division at a shallow tidal junction. *Water Resour Res* 46(12). doi:[10.1029/2010WR009266](https://doi.org/10.1029/2010WR009266)
- Dargahi B (2004) Three-dimensional flow modelling and sediment transport in the river Klaralven. *Earth Surf Process Landf* 29:821–852
- Deleersnijder E, Lermusiaux PFJ (2008) Multi-scale modelling: nested-grid and unstructured-mesh approaches. *Ocean Dyn* 58(5–6):335–336
- Deleersnijder E, Legat V, Lermusiaux PFJ (2010) Multi-scale modelling of coastal, shelf and global ocean dynamics. *Ocean Dyn* 60:1357–1359. doi:[10.1007/s10236-010-0363-6](https://doi.org/10.1007/s10236-010-0363-6)
- Dinehart R, Burau J (2005a) Averaged indicators of secondary flow in repeated Acoustic Doppler Current Profiler crossings of bends. *Water Resour Res* 41. doi:[10.1029/2005WR004050](https://doi.org/10.1029/2005WR004050)
- Dinehart R, Burau J (2005b) Repeated surveys by Acoustic Doppler Current Profiler for flow sediment dynamics in a tidal river. *J Hydrol* 314:1–21
- Edmonds D, Slingerland R (2007) Mechanics of river mouth bar formation: implications for the morphodynamics of delta distributary networks. *J Geophys Res*. doi:[10.1029/2006JF000574](https://doi.org/10.1029/2006JF000574)
- Friedrichs CT, Aubrey DG (1994) Tidal propagation in strongly convergent channels. *J Geophys Res* 99(C2):3321–3336
- Frigs RM, Kleinhans M (2008) Complex variations in sediment transport at three large river bifurcations during discharge waves in the river Rhine. *Sedimentology*. doi:[10.1111/j.1365-3091.2007.00940.x](https://doi.org/10.1111/j.1365-3091.2007.00940.x)
- Godin G (1991) Compact approximations to the bottom friction term, for the study of tides propagating in channels. *Cont Shelf Res* 11(7):579–589
- Godin G (1999) The propagation of tides up rivers with special considerations on the Upper Saint Lawrence River. *Estuar Coast Shelf Sci* 48:307–324
- Godin G, Martinez A (1994) Numerical experiments to investigate the effects of quadratic friction on the propagation of tides in a channel. *Cont Shelf Res* 14(7):723–748
- Hill AE, Souza AJ (2006) Tidal dynamics in channels: 2. Complex channel networks. *J Geophys Res* 111:C11021. doi:[10.1029/2006JC003670](https://doi.org/10.1029/2006JC003670)
- Hoitink AJF (2008) Comment on “The origin of neap-spring tidal cycles” by Erik P. Kvale [Marine Geology 235 (2006) 5–18]. *Ma Geol* 248(1–2):122–125. doi:[10.1016/j.margeo.2007.04.001](https://doi.org/10.1016/j.margeo.2007.04.001)
- Hoitink AJF, Buschman FA, Vermeulen B (2009) Continuous measurements of discharge from a Horizontal ADCP in a tidal river. *Water Resour Res* 45:W11406. doi:[10.1029/2009WR007791](https://doi.org/10.1029/2009WR007791)
- Jay DA (1997) Interaction of fluctuating river flow with a barotropic tide: a demonstration of wavelet tidal analysis methods. *J Geophys Res* 102:5705–5720
- Kvale E (2006) The origin of neap-spring tidal cycles. *Mar Geol* 235:5–18
- Lambrechts J, Comblen R, Legat V, Geuzaine C, Remacle J (2008a) Multiscale mesh generation on the sphere. *Ocean Dyn* 58(5–6):461–473
- Lambrechts J, Hanert E, Deleersnijder E, Bernard P, Legat V, Remacle J, Wolanski E (2008b) A multiscale model of the hydrodynamics of the whole Great Barrier Reef. *Estuar Coast Shelf Sci* 79:143–151
- Lane SN, Richards KS (1998) High resolution, two-dimensional spatial modelling of flow processes in a multi-thread channel. *Hydrol Process* 12:1279–1298
- LeBlond P (1979) Forced fortnightly tides in shallow rivers. *Atmos Ocean* 17(3):253–264
- Legleiter CJ, Kyriakidis PC (2007) Forward and inverse transformations between cartesian and channel fitted coordinate systems for meandering rivers. *Math Geol* 38:927–958
- Lutz G, Hubbell D, Stevens HJ (1975) Discharge and flow distribution, Columbia River estuary. Tech. rep., Geological Survey Professional Paper No., p 433
- Rennie C, Millar R, Church M (2002) Measurement of bed load velocity using an Acoustic Doppler Current Profiler. *J Hydraul Eng* 128:5:473–483
- Sassi M, Hoitink A, Vermeulen B, Hidayat (2011) Discharge estimation from H-ADCP measurements in a tidal river subject to sidewall effects and a mobile bed. *Water Resour Res* 47(W06504). doi:[10.1029/2010WR009972](https://doi.org/10.1029/2010WR009972)
- Simpson M (2001) Discharge measurements using a broad-band Acoustic Doppler Current Profiler. Tech. rep., United States Geological Survey
- Stein U, Alpert P (1993) Factor separation in numerical simulations. *J Atmos Sci* 50(4):2107–2115
- Wang Z, Fokkink R, de Vries M, Langerak A (1995) Stability of river bifurcations in 1D morphodynamic models. *J Hydraul Res* 33:739–750
- Warner JC, Schoellhamer D, Schladow G (2003) Tidal truncation and barotropic convergence in a channel network tidally driven from opposing entrances. *Estuar Coast Shelf Sci* 56(3–4):629–639
- Wolinsky MA, Edmonds DA, Martin J, Paola C (2010) Delta allometry: growth laws for river deltas. *Geophys Res Lett* 37:L21403. doi:[10.1029/2010GL044592](https://doi.org/10.1029/2010GL044592)
- Zanichelli G, Caroni E, Fiorotto V (2004) River bifurcation analysis by physical and numerical modeling. *J Hydraul Eng* 130(3):237–242